Structural evolution of iodine on approach to the monatomic state

Elena Bykova,[1,2] Iskander G. Batyrev,[3] Maxim Bykov [1,4] Eric Edmund,[1] Stella Chariton,[5]
Vitali B. Prakapenka [5] and Alexander F. Goncharov [1,4]

[1]*Earth and Planets Laboratory, Carnegie Institution for Science, Washington, DC 20015, USA*
[2]*Bayerisches Geoinstitut, University of Bayreuth, Universitätsstrasse 30, 95447 Bayreuth, Germany*
[3]*U.S. Army Research Laboratory, RDRLWML-B, Aberdeen Proving Ground, Maryland 21005, USA*
[4]*Institute of Inorganic Chemistry, University of Cologne, Greinstrasse 6, 50939 Cologne, Germany*
[5]*Center for Advanced Radiation Sources, The University of Chicago, Chicago, Illinois 60637, USA*

We applied single-crystal x-ray diffraction and Raman spectroscopy in a diamond-anvil cell up to 36 GPa and first-principles theoretical calculations to study the molecular dissociation of solid iodine at high pressure. Unlike previously reported, we find that the familiar $Cmce$ molecular phase transforms to a $Cmc2_1$ molecular structure at 16 GPa, and then to an incommensurate polymeric $Fmmm(00\gamma)s00$ structure, which can be viewed as a mixture of molecular I_2 and zigzag chains of three iodine atoms, at 20 GPa. The available data are consistent with metallization of iodine at the boundary between the commensurate $Cmc2_1$ structure and the incommensurate $Fmmm(00\gamma)s00$ structure at 20 GPa.

I. INTRODUCTION

Understanding pressure-driven dissociation of simple diatomic molecules is important for a range of topics including materials behavior under extremes and understanding the structure of planetary interiors. Such transformations, which are commonly preceded or accompanied by metallization, occur at very high pressures in the crystals made of light molecules (e.g., H_2 and F_2), where such investigations are very challenging [1,2]. However, molecular dissociation and band-gap closure occur at much lower pressures for heavier molecules. The halogens Cl_2, Br_2, and I_2 have been thoroughly investigated, revealing a common structural transition sequence [3–5], where molecular dissociation is reported to occur stepwise towards a simple monatomic structure. However, a fundamental question which has remained experimentally and theoretically challenging to address is the relationship between the metallization of the halogens and the dissociation of their constituent molecular unit. All studies agree that halogen metallization occurs prior to molecular dissociation (e.g., Refs. [3,4,6]), but it remains unclear whether metallization is related to a structural "step" on the transition pathway, or due to pressure-induced band overlap within the molecular solid.

Iodine has been investigated most extensively largely because it transforms to a metallic state at 1–24 GPa and experiences molecular dissociation at above 21 GPa [7–12]—conditions which are easily accessible with the diamond-anvil cell technique. Moreover, it shares a common transition sequence with the lighter halogens Cl_2 and Br_2. At low pressures, iodine crystallizes in an orthorhombic $Cmce$ structure [3] (phase I), which consists of flat layers, formed as associations of zigzag molecular chains (Fig. 1). Above 26 GPa, this structure transforms into a monatomic $Immm$ lattice (phase II), where iodine atoms occupy the corner sites forming a metallic

body-centered orthorhombic (BCO) single-atom unit cell [9]. However, careful investigations [13] showed the existence of an intermediate phase (V) at 24–26 GPa, which can coexist with the $Immm$ structure at 26–30 GPa. This intermediate structure can be viewed as a face-centered orthorhombic lattice based on the main diffraction peaks, but the occurrence of satellite reflections from both sides of the main peaks indicates the presence of an incommensurate modulation wave along the a axis, which shifts the atoms along the b axis. In this structure, there are three- or four-atom chains in the ab plane, with a continuous distribution of the nearest-neighbor interatomic distances covering a range of approximately 0.26 Å. Raman spectroscopy demonstrated the presence of a specific low-frequency soft mode for the modulated structures, called the amplitude mode (AM), which corresponds to transverse atomic vibrations and preserves the symmetry of the modulation wave [5]. No Raman signal has been detected in phase II as expected from the Raman selection rules.

In the stepwise molecular dissociation scenario presented above, it remains puzzling if molecular phase I metallizes via band overlap and whether there is any indication of its instability toward the transformation into modulated phase V or any other structural modification. Indeed, theoretical calculations predict such instability within $Cmce$ structure due to a coupling of the bond charge density with a transverse optical phonon [15]. Raman measurements of phase I [5,16] demonstrated the presence of $2A_g + 2B_{3g}$ in-plane stretching (S) and librational (L) modes, out of which $A_g(L)$ mode turns over and becomes a soft mode above 13 GPa. In the same pressure range, additional Raman modes appear that cannot be explained within the Raman selection rules of $Cmce$ structure. In addition, Mössbauer experiments demonstrated an anomaly at 16 GPa suggesting a phase transformation [17], while x-ray absorption spectroscopy showed a hint of an increase in the intramolecular bond distance in the same pressure range [4].
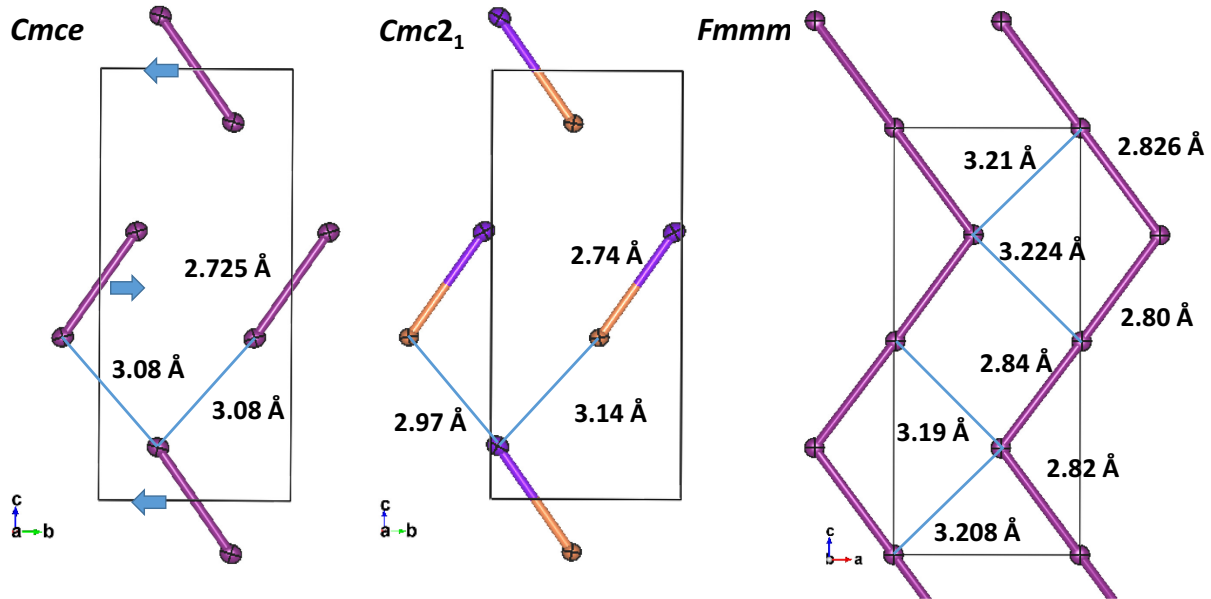
FIG. 1. Fragments of crystal structures of *Cmce* (I), *Cmc*2_1 (VI), and *Fmmm*$(00\gamma)s00$ (VII) phases determined in this work (Table I and Table S1 of Supplemental Material [14]) projected to *bc* (*ac* for *Fmmm*) plane. Atoms occupying different crystallographic sites are shown in different colors. Atoms are represented by displacement ellipsoids (at 75% probability) as they occur after structural refinement. Arrows show directions of shifts of molecular layers that occur at *Cmce* to *Cmc*2_1 transition. *Fmmm*$(00\gamma)s00$ structure presentation is approximate (small unit cell) (see detailed structural results in Table S1 [14]).

Theoretical first-principles calculations [18] suggested that there is another molecular phase (phase I′), which has *C2/m* symmetry; it was proposed to coexist with *Cmce* phase I [18]. This phase has two types of I_2 molecules in the unit cell with different intramolecular lengths offering an explanation to the extra Raman bands, which appear above 14 GPa.

Here, we present the results of concomitant synchrotron single-crystal (SC) x-ray diffraction (XRD) and Raman measurements, which provide a detailed structural description of the multistage molecular dissociation of iodine. Our experiments unequivocally identify intermediate phases——a *Cmc*2_1 molecular phase (hereafter I_2-VI, cf. Ref. [19]), and an incommensurate *Fmmm*$(00\gamma)s00$ phase (hereafter I_2-VII) characterized by the loss of well-defined stable molecules. We infer that the VI-VII structural transformation is responsible for pressure-induced metallization reported previously. Our first-principles theoretical calculations show that *Cmc*2_1 I_2-VI phase is energetically competitive, dynamically stable, and confirms the presence of the additional Raman bands as due to the reduction in symmetry upon transition to the *Cmc*2_1 phase.

II. MATERIALS AND METHODS

A. Experiments

The experimental procedure included concomitant SC XRD and Raman spectroscopy [20] measurements at 10–36 GPa in the GeoSoilEnviroCARS (GSECARS), Sector 13 of the Advanced Photon Source, Argonne National Laboratory. Samples in the form of flakes were placed in a cavity of a diamond-anvil cell formed in a central hole made in a preindented rhenium gasket, sealed to avoid sublimation, and then loaded by compressing Ne gas to 160 MPa at room temperature. Ruby served as an optical pressure gauge, while

the equation of state of Ne [21] has been used to cross check pressure during XRD measurements. Compressed Ne serving as a pressure medium provided quasihydrostatic conditions in the high-pressure cavity, as witnessed by SC XRD data, which were of sufficiently high quality up to at least 27 GPa. At this pressure we performed laser annealing of the sample up to 1800 K to improve the quality of SC XRD data as will be presented below. Additional Raman measurements have been collected at Earth and Planets Laboratory of the Carnegie Institution for Science, before and after synchrotron XRD experiments.

For single-crystal XRD measurements at GSECARS, we used monochromatic x-ray radiation with $\lambda = 0.2952$ Å focused down to $3 \times 3\, \mu m^2$ by a Kirkpatrick-Baez mirror system, and diffraction patterns were collected on a Pilatus 1M detector (CdTe). Diffraction images were measured by a Pilatus 1M (CdTe) pixel detector. For the single-crystal XRD measurements, samples were rotated around a vertical ω axis in a range of $\pm 35°$ with an angular step $\Delta \omega = 0.5°$ and an exposure time of 1–2 seconds per frame. For analysis of the single-crystal diffraction data we used the CRYSALISPRO software package, which allows to perform the SC XRD analysis for multigrain samples. To calibrate an instrumental model in the CRYSALISPRO software, i.e., the sample-to-detector distance, detector's origin, offsets of goniometer angles, and rotation of both x-ray beam and the detector around the instrument axis, we used a single crystal of orthoenstatite $((Mg_{1.93}Fe_{0.06})(Si_{1.93}, Al_{0.06})O_6$, *Pbca* space group, $a = 8.8117(2)$, $b = 5.1832(1)$, and $c = 18.2391(3)$ Å). The structures were solved with the SHELXT structure solution program and refined with the OLEX2 program [22,23]. The Cambridge Structural Database contains the supplementary crystallographic data for this work. These data can be obtained

TABLE I. Crystal structure details of commensurate phases of iodine.

Pressure, GPa	9.90	15.0	17.0	19.0	32.0
Space group	$Cmce$	$Cmce$	$Cmc2_1$	$Cmc2_1$	$Immm$
Phase	Iodine-I	Iodine-I	Iodine-VI	Iodine-VI	Iodine-II
Pressure step	p01	p02	p03	p04	p08
a (Å)	6.163(4)	5.978(4)	5.908(5)	5.829(6)	2.9077(6)
b (Å)	4.1435(3)	4.0396(4)	4.0055(3)	3.9773(6)	3.0333(12)
c (Å)	9.2864(8)	9.1487(9)	9.0992(11)	9.0739(13)	5.226(7)
Z	2	2	2	2	2
V (Å^3)	237.15(16)	220.94(15)	215.3(2)	210.4(2)	46.10(7)
ρ_{calc} (g/cm^3)	7.109	7.63	7.83	8.014	9.143
μ/mm^{-1}	13.804	20.519	15.204	15.563	17.755
$2\Theta_{\text{min}}$ for data collection (°)	2.624	3.549	3.158	2.575	6.508
$2\Theta_{\text{max}}$ for data collection (°)	14.627	15.055	15.001	14.776	13.102
Completeness to $d = 0.8$ Å	0.527	0.468	0.432	0.545	0.25
Reflections collected	259	165	243	327	21
Independent reflections	136	86	175	213	16
Independent reflections [$I > 2\sigma(I)$]	132	80	171	213	15
Refined parameters	7	7	13	13	4
$R_{\text{int}}(F^2)$	0.012	0.0131	0.0124	0.0087	0.083
$R(\sigma)$	0.0148	0.0097	0.0163	0.0126	0.0316
R_1 [$I > 2\sigma(I)$]	0.0356	0.0246	0.031	0.0351	0.0836
wR_2 [$I > 2\sigma(I)$]	0.1028	0.0606	0.0784	0.0922	0.1911
R_1	0.0368	0.026	0.0315	0.0351	0.0826
wR_2	0.1057	0.0626	0.0785	0.0922	0.1907
Goodness of fit on F^2	1.201	1.139	1.1	1.164	1.308
$\Delta\rho_{\text{max}}(e/\text{Å}^3)$	1.774	1.068	1.463	2.02	2.874
$\Delta\rho_{\text{min}}(e/\text{Å}^3)$	−1.579	−0.825	−1.096	−1.807	−2.468
x(I 1)	0	0	0	0	0
y(I 1)	0.18376(9)	0.19087(6)	0.4299(2)	0.4306(3)	0
z(I 1)	0.62197(4)	0.62278(3)	0.26446(10)	0.26390(15)	0
U_{eq}(I 1) (Å^2)[a]	0.0165(6)	0.0099(6)	0.0080(9)	0.0086(9)	0.011(5)
x(I 2)			0	0	
y(I 2)			0.0387(3)	0.0291(6)	
z(I 2)			0.51173(10)	0.51229(15)	
U_{eq}(I 2) (Å^2)[a]			0.0096(9)	0.0114(10)	

[a]U_{eq} is defined as one-third of the trace of the orthogonalized U_{ij} tensor.

free of charge from FIZ Karlsruhe (deposition numbers CSD 2283235-2283239) [24].

B. Theoretical calculations

First-principles theoretical calculations have been performed in $Cmce$, $Cmc2_1$, $C2/m$, and $Immm$ phases at selected pressures between 0 and 30 GPa, where these structures were optimized using norm-conserving pseudopotentials, generalized gradient approximations (GGA)-Perdew-Burke-Ernzerhof (PBE) functional, and GRIMME2 dispersion corrections [25]. Monkhorst-Pack grid size for k-point sampling of the Brillouin zone is $5\times6\times5$ for all structures except I$_2$-II ($Immm$) at 30 GPa, where $6\times7\times6$ sampling was used [26]. The phonon dispersion and phonon frequency calculations were performed using a finite-displacement method implemented in the CASTEP code [27]. The Raman spectra were calculated using the formalism presented in Ref. [28]. Since application of GGA-PBE functional incorrectly predicts that $Cmce$ phase is thermodynamically and dynamically unstable at 0 GPa [29], we performed calculations using Minnesota

2006 local functional [30] (M06-L) in $Cmce$ and $Cmc2_1$ phases up to 30 GPa. The electronic band-gap calculations have been performed within GGA/PBE and PBE-based screen hybrid functional Heyd-Scuseria-Ernzerhof (HSE06) [31] approximations.

III. RESULTS AND DISCUSSION

Up to 15 GPa SC XRD patterns confirm the previously reported $Cmce$ structure (Table I). However, SC XRD measurements at 17 GPa demonstrate a difference in the x-ray extinction rules. Reflections ($h\ k\ 0$), with $h = 2n + 1$ and $k = 2n + 1$ [e.g., (1 3 0), (1 5 0), and others] appear in the diffraction patterns (Fig. 2). These weaker reflections cannot be observed in powder XRD patterns as they are much weaker than the main ones ($<0.1\%$) and interfere with stronger reflections, so this symmetry change was previously overlooked. A structure can be indexed with the $Cmc2_1$ space group, which represents a subgroup of the $Cmce$ group. The structural distortion in the $Cmc2_1$ I$_2$-VI structure is very subtle (Fig. 1). It can be understood as a small shift of layers of
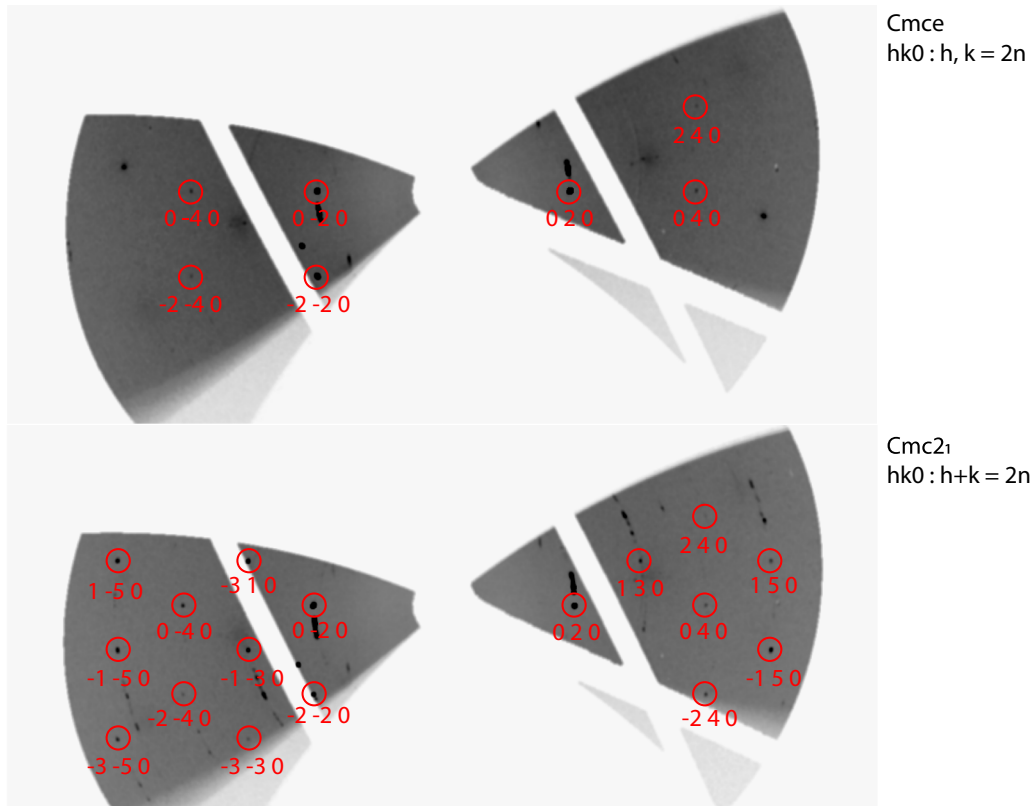
FIG. 2. Reconstructed reciprocal lattice planes of iodine at 15 GPa (upper panel) and at 17 GPa (lower panel). Observed diffraction spots from sample have been indexed and used to determine structure of *Cmce* (I_2-I) and *Cmc*2_1 (I_2-VI) phases, respectively (see details in Table I). X-ray extinctions rules for these phases are depicted.

collinear molecules along the *b* axis, which diminishes the lattice symmetry.

On further compression, above 20 GPa, yet another subtle change in symmetry occurs (Figs. 1 and 3). At this point, a stable structural solution within *Cmc*2_1 space group is not possible. A sequence of diffraction spots from (0*kl*) lattice planes (Fig. 3) shows a splitting of several reflections along the c^* direction at 20.8 GPa, manifesting the occurrence of an incommensurate lattice with a modulation vector of $q = 0.4837(2)$. An incommensurate phase has $Fmmm(00\gamma)s00$ structure, which is isosymmetrical with phase V at higher pressures. The existence of this phase is consistent with Ref. [19], where this phase was reported at 16–23 GPa. In contrast, we find no incommensurate structure below 20 GPa, where commensurate *Cmc*2_1 I_2-VI is stable. Both commensurate *Cmc*2_1 and *Cmce* are the $a \times b \times 2c$ super-cell subgroups of $Fmmm(00\gamma)s00$ with $\gamma = 0.5$ and various initial phases of modulation t_0 (1/8 for *Cmce* and general for *Cmc*2_1).

In incommensurate I_2-VII phase, the nearest-neighbor interatomic distances are modulated (Fig. S1 of Supplemental Material [14]) spreading a wide range, which covers typical intra-to-intermolecular I-I distances. This phase consists of a dynamic mixture of molecular I_2 and polymeric zigzag chains of three I atoms (see also Ref. [19]) in the *ac* plane (Fig. S2 of Supplemental Material [14]).

Our concomitant Raman measurements below 24 GPa demonstrate smooth changes with pressure (Fig. 4), which

are generally consistent with previous observations [5,16]. Above 16 GPa, where *Cmc*2_1 I_2-VI is documented in XRD, peaks appear, dubbed *X* and *Y* in the literature, with the frequencies below $A_g(L)$ and above $B_{3g}(L)$ modes, respectively. The appearance of these modes can be understood by the Raman selection rule modification at the *Cmce* → *Cmc*2_1 phase transition (Table II); the most prominent difference in *Cmc*2_1 phase VI is the relaxation of the rule of mutual exclusion for the Raman and IR active modes. According to group-theory predictions, all optical modes are Raman active in phase VI, out of which the most intense $3A_1 + 3B_2$ in-plane modes are expected to be observed in Raman spectra compared to $2A_g + 2B_{3g}$ modes of *Cmce* phase I. We note that *X* and *Y* modes are coupled to $A_g(L)$ and $B_{3g}(L)$ originated modes, respectively. This is evident from their frequency curves vs pressure [Fig. 4(b)], which show characteristic avoided-crossing dependencies and an exchange in intensities correlated with the frequency approaching as in the case of Fermi resonance. This behavior shows that the coupled modes are of the same symmetry, namely A_1 and B_1 modes of *Cmc*2_1 phase [Fig. 4(b)]. Thus, the appearance and behavior of the *X* and *Y* modes are well understood by the *Cmce* → *Cmc*2_1 phase transformation; these modes originate from IR-active $B_{1u} + B_{2u}$ modes of *Cmce* phase, which become Raman active in *Cmc*2_1 phase (Table II). These modes correspond to translational motions of I_2 molecules along the *b*- and *c* axes, which couple with librational motions in phase VI.
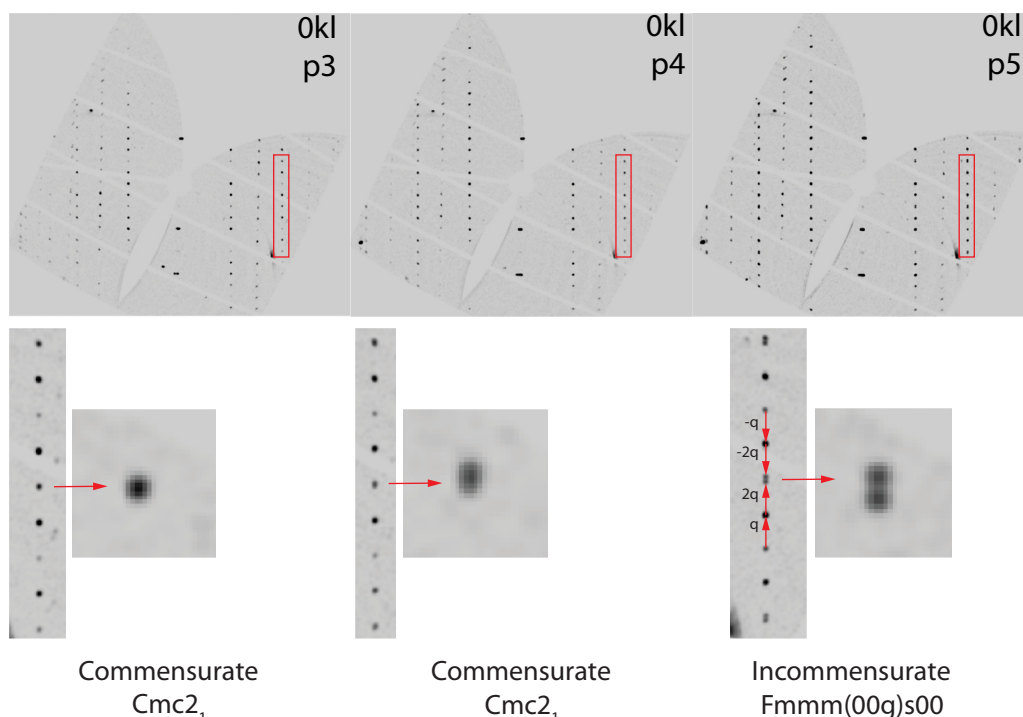
FIG. 3. Reconstructed reciprocal lattice planes of iodine at 17, 19, and 20.8 GPa (from left to right). Insets below show enlarged views of Bragg peaks marked by red rectangles. Splitting of zoomed-in peak manifests occurrence of incommensurate phase at 20.8 GPa.

Only subtle changes (mainly peak broadening) occur in the Raman spectra above 20 GPa, where our XRD data indicate a transition into an incommensurate $Fmmm(00\gamma)s00$ I_2-VII phase. The presence of vibrational modes characteristic for molecular phases is likely because this phase still consists of short-lived I_2 molecules demonstrating fluxional

behavior, which is supported by molecular-dynamics simulations of Ref. [19]. This behavior is consistent with the incommensurate nature of this phase, where molecular breakdown and recombination are associated with the modulation wave propagating through the crystal. It is the instantaneous existence of molecules that leads to a Raman response similar
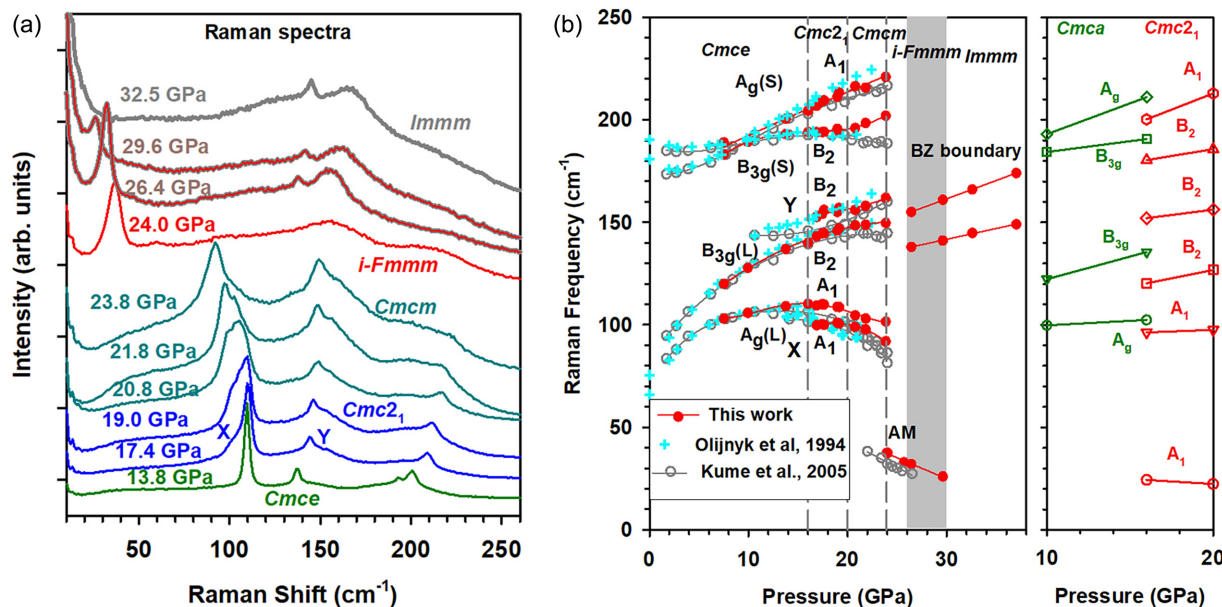

FIG. 4. Raman spectroscopy data. Panel (a) shows sequence of Raman spectra across phase transitions on pressure increase. Phase symmetries are labeled, and traces are color coded. Modes labeled as X and Y appear in $Cmc2_1$ phase and gain intensity. Panel (b) shows pressure dependencies of Raman frequencies measured here and compared to previous investigations [5,16] (left panel) as well as theoretically calculated (right panel) in this work.

TABLE II. Vibrational modes and their Raman and IR activity in *Cmce* and *Cmc*2_1 crystal structures.

Space and point group	*Cmce* No. 64 (D_{2h})		*Cmc*2_1 No. 36 (C_{2v})	
Site symmetry	$8f$ (C_S)		$4a +4a$ (C_S)	
Acoustic modes	$B_{1u} + B_{2u} + B_{3u}$		$A_1 + B_1 + B_2$	
Optical modes	Modes	Activity	Modes	Activity
	A_u	Silent	A_2	Raman
	$B_{1u} + B_{2u} + B_{3u}$	IR	$A_1 + B_2 + B_1$	IR and Raman
	$B_{1g} + B_{2g}$	Raman (*a*)	$A_2 + B_1$	Raman and IR
	$2A_g + 2B_{3g}$	Raman (*bc*)	$2A_1 + 2B_2$	Raman and IR

to that of *Cmce* and *Cmc*2_1 phases. At 23.8 GPa, the A_1 mode originated from the *X* mode becomes a dominant mode in the spectrum; this mode is a soft one corresponding to librational motions of I_2 molecules with the eigenvector, which captures the pathway to a monatomic lattice. The mode behavior observed here is qualitatively consistent with the first-principles theoretical calculations (Fig. 4(b) and Fig. S3 of Supplemental Material [14]).

Our first-principles theoretical calculations show that *Cmc*2_1 phase is energetically favorable with respect to *Cmce*, *C2/m*, and *Cmcm* (local structure for incommensurate phase VII) in the pressure range above 15 GPa, where *Cmce* phase is reported to transform in this work and Refs. [18,19] (Fig. 5). However, within GGA-PBE approximation, *Cmc*2_1 phase is substantially more stable than the experimental *Cmce* ground-state phase below 15 GPa (see also Ref. [29]), which clearly contradicts the experiments. This apparent inconsistency is removed if M06-L functional is used as the enthalpies of *Cmce* and *Cmc*2_1 phases become nearly degenerate in the whole pressure range of interest. Both these phases are dynamically

stable at 5–30 GPa as witnessed by calculations of the phonon dispersion curves (Fig. S4 of Supplemental Material [14]). GGA-PBE calculations of the electronic band structure show that the molecular phases determined here are semiconducting with narrow band gaps decreasing with pressure, which are expected to close at 26 GPa (Fig. 6). This result is in a qualitative agreement with the results of HSE06 hybrid functional band-gap calculations, which show slightly larger values for the band gaps and the band-gap closure at 24 GPa in both phases.

At 24 GPa, XRD patterns and Raman spectra change abruptly. SC XRD performed in this work find a modulated structure (Fig. 7, Fig. S5, and Table S2 [14]) as reported in Ref. [13] based on powder-diffraction data (phase V). Unlike Ref. [13], we find the structure of phase V to be $Fmmm(00\gamma)s00$ (cf. $Fmm2(a00)0s0$ in Ref. [13]) in agreement with the more recent analysis [32]. We also find that the modulation vector value decreases with pressure (Fig. S6 of Supplemental Material [14]) in agreement with Refs. [13,32]. However, we additionally find, based on SC XRD measurements on high-quality laser-annealed crystals (Fig. 7), that there is a tiny atomic displacement along the *c* axis (Table S2 [14]). Overall, these results definitively establish the structure
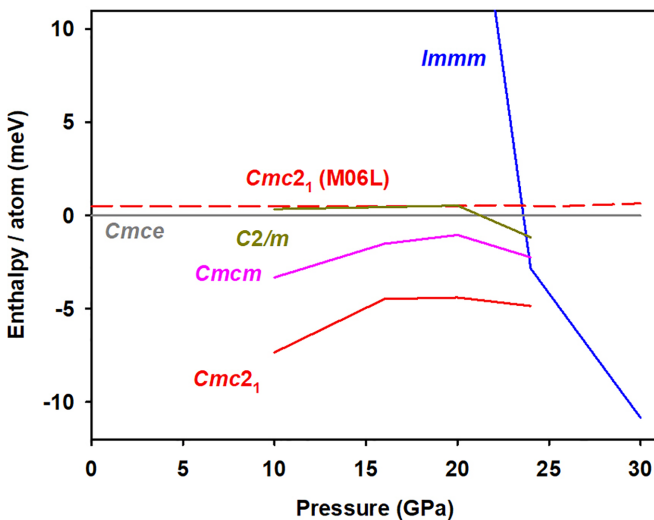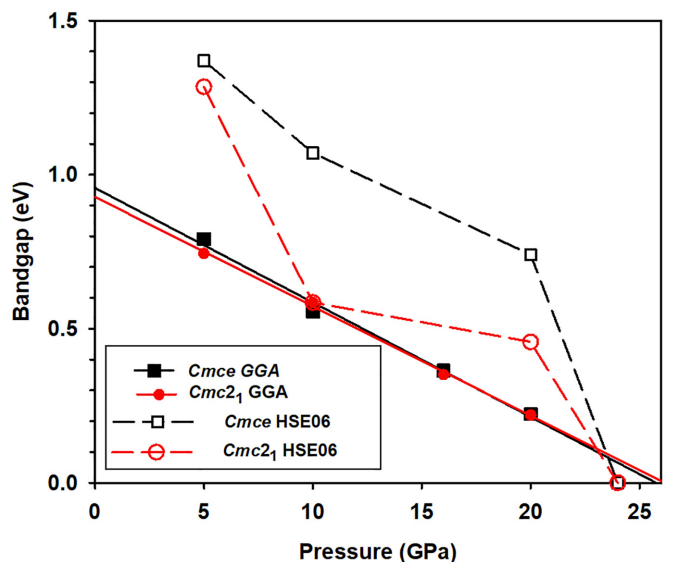

FIG. 5. Theoretically computed enthalpies of candidate phases vs pressure determined here from first principles plotted with respect to results for *Cmce* phase. Solid lines are results computed using GGA-PBE functional, while a dashed line for *Cmc*2_1 phase is obtained using Minnesota 2006 local functional (M06-L). Computed equilibrium phases are dynamically stable in pressure range presented here.

FIG. 6. Electronic band gap calculated as a function of pressure in *Cmce* and *Cmc*2_1 structures in GGA/PBE and HSE06 approximations.
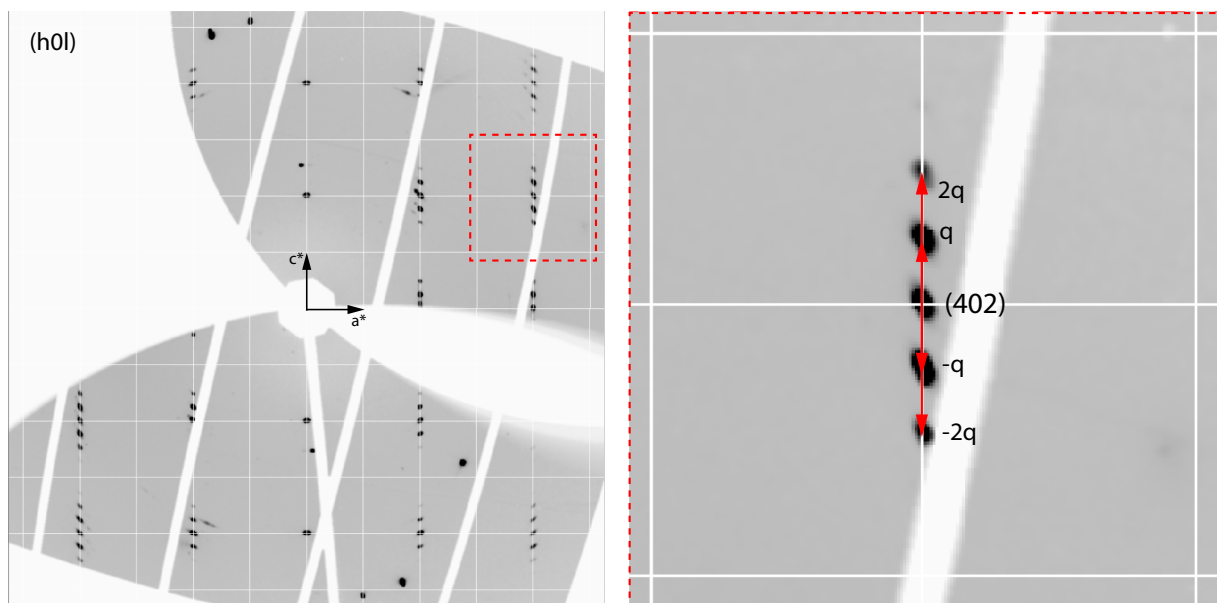
FIG. 7. Reconstructed reciprocal lattice planes of iodine phase V at 26.4 GPa. Right panel shows enlarged view of fine structure near (402) reflection of parent $Fmmm$ phase. Satellite reflections are indexed in terms of modulation vector. Details of structural refinement are presented in Table S2 of Supplemental Material [14]).

of a modulated phase V proposed in Ref. [13]. However, our data do not support the tetragonal five-dimensional modulated structure $[I4/mmm(\alpha\alpha0)000s(-\alpha\alpha0)0000]$ proposed in Ref. [19]. As can be seen in the reconstructed precession image (Fig. 7), there is only one modulation vector, which can describe all the satellite reflections.

Raman spectra above 24 GPa do not show any modes of the lower-pressure molecular phases I, VI, and VII. Instead, a strong soft Raman mode appears at low frequencies, which has been previously identified as an AM [5] (Fig. 4). These observations confirm that the modulated phase V is incommensurate, where the Brillouin-zone center vibrational modes of the parent phase are forbidden. Above 26 GPa, two Raman excitations, a narrow one and a broad one at nearly $150\,\text{cm}^{-1}$, appear and shift to higher frequencies with pressure (Fig. 4). Monatomic (BCO) phase II coexists with phase V in this regime, identified in powder XRD measurements. Above 30 GPa, the AM mode disappears, and XRD measurements show a single-phase BCO structure. Based on our theoretical calculations (Fig. S7 [14]), the Raman bands observed in this phase correspond well in frequency and pressure shift to the Brillouin-zone boundary transverse acoustic modes near the R, W, and T points, where the corresponding dispersion curves are flat, yielding sharp maxima in the phonon density of states at 4 THz ($134\,\text{cm}^{-1}$). The mechanism of their Raman activity (e.g., defect induced) is not clear at this stage.

Our results show the presence of an intermediate molecular phase VI and fluxional mixed molecular-zigzag incommensurate phase VII between a low-pressure molecular phase I and a modulated and dynamically dissociated phase V. Phase VI has $Cmc2_1$ orthorhombic symmetry, which can be described as a small distortion of $Cmce$ low-pressure phase. This phase can be viewed as a slightly dissociated (with longer intramolecular distance (Figs. 1 and 8) molecular phase, where

intermolecular coupling has been modified to approach zigzag chains of three iodine atoms. Previous experiments and theoretical calculations proposed a monoclinic $C2/m$ structure in this regime [18], but our XRD experiments clearly rule out this phase. In a recent work, it has been proposed that phase VI is a modulated incommensurate phase [19]; however, our
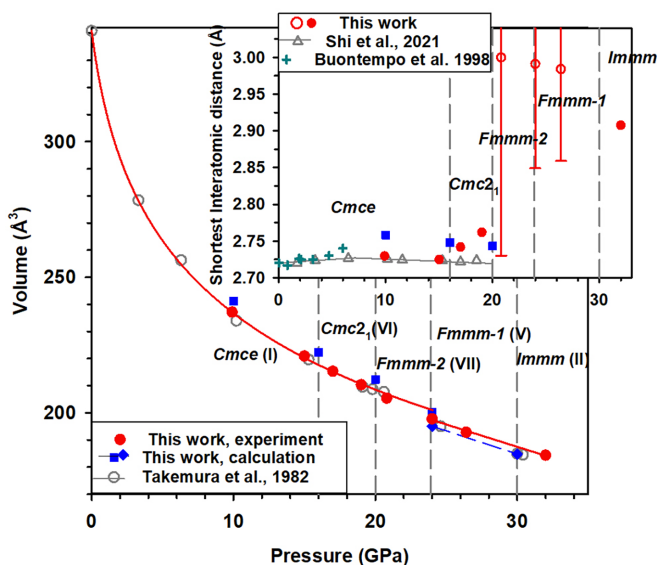

FIG. 8. Volume compression of iodine. Inset shows nearest interatomic distance vs pressure data. Results of this work (filled symbols, the uncertainty is smaller than symbol size) are compared to previously reported data (open symbols and crosses) from Refs. [4,9,33]. Solid line extrapolated to transition into modulated $Fmmm$ phase is a Vinet fit to our data [$V_0 = 340.9(2)$ Å^3 [3], $K_0 = 8.1(5)$, and $K'_0 = 7.0(3)$, where K_0 and K'_0 are bulk modulus and its pressure derivative at $P = 0$]. Vertical bars in inset show spread of nearest I-I distances in incommensurate phases.

SC XRD data clearly show that no satellite reflections are observed below 20 GPa. In a qualitative agreement with the results of previous works [13,19,32], we find the structure of phase V at 24–30 GPa to be modulated and incommensurate (Fig. 7 and Figs. S5 and S6 of Supplemental Material [14]); however, the symmetry and the dimensionality are different from that proposed in Ref. [19].

Our phase identification is consistent with Mössbauer experiments [17], which proposed a change in symmetry based on discontinuous changes in the electric-field gradient (EFG) parameters. We theoretically computed these parameters in $Cmce$ and $Cmc2_1$ phases and found discontinuous changes in EFG, which are qualitatively consistent with the Mössbauer observations (Fig. S8 [14]).

The $Fmmm(00\gamma)s00$ incommensurate mixed molecular-zigzag phase VII differs from incommensurate phase V in that the latter one can be viewed as totally dissociated, consisting of I_4 and I_5 zigzag atomic chains (Figs. S1 and S2), while phase VII still has a large disparity between intra- and intermolecular bond lengths, which results in formation of zigzag I_3 chains (cf. Ref. [19]), while some I_2 molecules still remain. The modulation vector of phase VII is substantially larger than that of phase V (Fig. S6). The interatomic distances in both modulated phases V and VII greatly vary (Fig. 8, Fig. S1), while the average distance decreases with pressure due to the volume compression. The structural sequence observed here of commensurate ($Cmce$)→ commensurate($Cmc2_1$)→ incommensurate $Fmmm(00\gamma)s00$ ($\gamma \sim 0.5$)→ incommensurate $Fmmm(00\gamma)s00$ ($\gamma \sim 0.25$)→ $Immm$ describes a seamless pathway for the molecular dissociation of I_2. While molecular broken-symmetry $Cmc2_1$ phase VI is semiconducting based on its nature and theoretical calculations, a structural distortion in incommensurate phase VII must be of electronic nature; this indicates that metallization occurs via a structural transformation between these two phases.

Our XRD data also address the volume change at metallization and molecular dissociation transition (Fig. 8). There is no measurable volume change at the $Cmce \rightarrow Cmc2_1$ (VI)→ $Fmmm(00\gamma)s00$ (VII) phase transitions. However, there is a volume collapse of 1.8% that occurs at the isosymmetrical VII-V transition [both have $Fmmm(00\gamma)s00$ symmetry] (cf. Ref. [13]). This is smaller than that theoretically computed

here using density-functional theory calculations using GGA-PBE functional (4.2%). It has been previously suggested that metallization occurs continuously via band-gap closure in a molecular state, thus preceding dissociation [4]. Based on our XRD results and theoretical calculations of the electronic structure (Figs. S3, S4), we suggest that the $Cmc2_1 \rightarrow Fmmm(00\gamma)s00$ (VII) phase transitions at 20 GPa can be directly connected to metallization reported at 14–24 GPa [10]. In this case, there is no volume collapse associated with metallization. Molecular dissociation occurs stepwise from truly molecular $Cmce$ and $Cmc2_1$ to dynamically disordered $Fmmm(00\gamma)s00$ and dynamically dissociated i-$Fmmm$ phase. It would be of great interest to investigate if these results, especially the existence of intermediate phases $Cmc2_1$ phase VI and $Fmmm(00\gamma)s00$ phase VII, are applicable to Br_2 and Cl_2, which were reported to have a similar structural behavior.

[1] A. Goncharov, Low Temp. Phys. **46**, 97 (2020).

[2] E. Gregoryanz, C. Ji, P. Dalladay-Simpson, B. Li, R. T. Howie, and H.-K. Mao, Matter Radiat. Extremes **5**, 038101 (2020).

[3] H. Fujihisa, Y. Fujii, K. Takemura, and O. Shimomura, J. Phys. Chem. Solids **56**, 1439 (1995).

[4] J. Shi, E. Fonda, S. Botti, M. A. L. Marques, T. Shinmei, T. Irifune, A.-M. Flank, P. Lagarde, A. Polian, J.-P. Itié, and A. San-Miguel, Phys. Chem. Chem. Phys. **23**, 3321 (2021).

[5] T. Kume, T. Hiraoka, Y. Ohya, S. Sasaki, and H. Shimizu, Phys. Rev. Lett. **94**, 065506 (2005).

[6] P. Dalladay-Simpson, J. Binns, M. Peña-Alvarez, M.-E. Donnelly, E. Greenberg, V. Prakapenka, X.-J. Chen, E. Gregoryanz, and R. T. Howie, Nat. Commun. **10**, 1134 (2019).

[7] R. W. Lynch and H. G. Drickamer, J. Chem. Phys. **45**, 1020 (1966).

[8] K. Takemura, S. Minomura, O. Shimomura, and Y. Fujii, Phys. Rev. Lett. **45**, 1881 (1980).

[9] K. Takemura, S. Minomura, O. Shimomura, Y. Fujii, and J. D. Axe, Phys. Rev. B **26**, 998 (1982).

[10] T. Ishikawa, K. Mukai, Y. Tanaka, M. Sakata, Y. Nakamoto, T. Matsuoka, K. Shimizu, and Y. Ohishi, High Pressure Res. **33**, 186 (2013).

[11] A. S. Balchan and H. G. Drickamer, J. Chem. Phys. **34**, 1948 (1961).

[12] N. Sakai, K.-I. Takemura, and K. Tsuji, J. Phys. Soc. Jpn. **51**, 1811 (1982).

[13] T. Kenichi, S. Kyoko, F. Hiroshi, and O. Mitsuko, Nature (London) **423**, 971 (2003).

[14] See Supplemental Material at http://link.aps.org/supplemental/10.1103/PhysRevB.108.024104 for Supplemental Figs. S1–S8, and Tables S1 and S2.

[15] T. Luty and J. C. Raich, Can. J. Chem. **66**, 812 (1988).

[16] H. Olijnyk, W. Li, and A. Wokaun, Phys. Rev. B **50**, 712 (1994).

[17] M. Pasternak, J. N. Farrell, and R. D. Taylor, Phys. Rev. Lett. **58**, 575 (1987).

[18] Q. Zeng, Z. He, X. San, Y. Ma, F. Tian, T. Cui, B. Liu, G. Zou, and H.-K. Mao, Proc. Natl. Acad. Sci. USA **105**, 4999 (2008).

[19] H. Fujihisa, K. Takemura, M. Onoda, and Y. Gotoh, Phys. Rev. Res. **3**, 033174 (2021).

[20] N. Holtgrewe, E. Greenberg, C. Prescher, V. B. Prakapenka, and A. F. Goncharov, High Pressure Res. **39**, 457 (2019).

[21] Y. Fei, A. Ricolleau, M. Frank, K. Mibe, G. Shen, and V. Prakapenka, Proc. Natl. Acad. Sci. USA **104**, 9182 (2007).

[22] G. Sheldrick, Acta Cryst. A **71**, 3 (2015).

[23] O. V. Dolomanov, L. J. Bourhis, R. J. Gildea, J. A. K. Howard, and H. Puschmann, J. Appl. Cryst. **42**, 339 (2009).

[24] www.ccdc.cam.ac.uk/structures.

[25] D. R. Hamann, M. Schlüter, and C. Chiang, Phys. Rev. Lett. **43**, 1494 (1979).

[26] H. J. Monkhorst and J. D. Pack, Phys. Rev. B **13**, 5188 (1976).

[27] K. Refson, P. R. Tulip, and S. J. Clark, Phys. Rev. B **73**, 155114 (2006).

[28] D. Porezag and M. R. Pederson, Phys. Rev. B **54**, 7830 (1996).

[29] J. George, C. Reimann, V. L. Deringer, T. Bredow, and R. Dronskowski, ChemPhysChem **16**, 728 (2015).

[30] Y. Zhao and D. G. Truhlar, J. Chem. Phys. **125**, 194101 (2006).

[31] O. A. Vydrov, J. Heyd, A. V. Krukau, and G. E. Scuseria, J. Chem. Phys. **125**, 074106 (2006).

[32] K. Takemura, K. Sato, H. Fujihisa, and M. Onoda, Z. Kristallogr. **219**, 749 (2004).

[33] U. Buontempo, A. Filipponi, D. Martínez-García, P. Postorino, M. Mezouar, and J. P. Itié, Phys. Rev. Lett. **80**, 1912 (1998).